Interleaved Half-Bridge Flyback Converter With Zero-Current Switching

Tsorng-Juu Liang, *Fellow, IEEE*, Ming-Hsien Cheng, Wen-Yu Huang, and Wei-Jing Tseng

***Abstract*—Conventional interleaved half-bridge flyback converters can recycle the leakage energy stored in leakage inductance to clamp the voltage across the main power switches at a dc input voltage. However, such converters still suffer from high switching losses, especially turn-OFF losses. In this paper, a novel turn-OFF zero-current-transition (ZCT) circuit is proposed for reducing the turn-OFF switching losses. The proposed ZCT interleaved half-bridge flyback converter operates at a fixed frequency without increasing the voltage stresses of the main switches. To verify the design, a laboratory prototype is implemented with 100 kHz, an input voltage of 400 V, and an output voltage of 24 V/480 W. The experimental results reveal that the proposed converter at full load and 20% load has efficiencies of 93.05% and 89.06%, yielding efficiency improvements of 1.17% and 4.12%, respectively, compared with the conventional interleaved half-bridge flyback converter.**

***Index Terms*—Half-bridge flyback converter, turn-OFF switching losses, zero-current switching (ZCS), zero-current transition (ZCT).**

I. Introduction

FOR safety considerations, it is necessary to apply electric isolation between the input and output of a power converter. In switching mode power supplies, flyback converters are widely used in isolated low-power supplies due to their compact topology, multioutput applications, and simple control. Nevertheless, resonance between the leakage inductance of the flyback transformer and the switch capacitance causes high-voltage stress on the switch during the switch-OFF period. As a consequence, the converter needs either a clamp circuit to suppress the voltage stress on the switch or higher-rated components to bear the high-voltage stress on the switch; otherwise, the voltage spikes will damage the devices. Usually, snubber circuits can suppress such high-voltage spikes on the power switch; however, in doing so, the snubber resistor dissipates the leakage energy, which reduces the converter's efficiency [1].

Manuscript received March 21, 2018; revised May 16, 2018; accepted June 18, 2018. Date of publication July 1, 2018; date of current version February 20, 2019. This work was supported in part by the Power Electronics Fundamental Technology Develop Center from the Ministry of Science and Technology (MOST), Taiwan and in part by the Hierarchical Green-Energy Materials (Hi-GEM) Research Center, from The Featured Areas Research Center Program within the framework of the Higher Education Sprout Project by the Ministry of Education (MOE), Taiwan. Recommended for publication by Associate Editor Prof. X. Ruan. *(Corresponding author: Tsorng-Juu Liang.)*

The authors are with the Department of Electrical Engineering and Hierarchical Green-Energy Materials Research Center, National Cheng Kung University, Tainan, 70101 Taiwan, R.O.C. (e-mail:

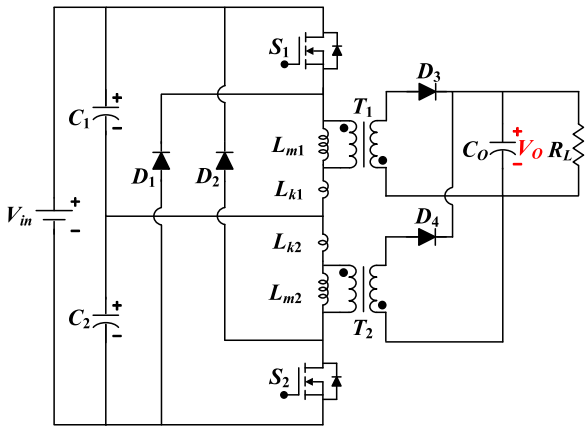

Fig. 1. Conventional IHBFC with recycled leakage energy [4], [5].

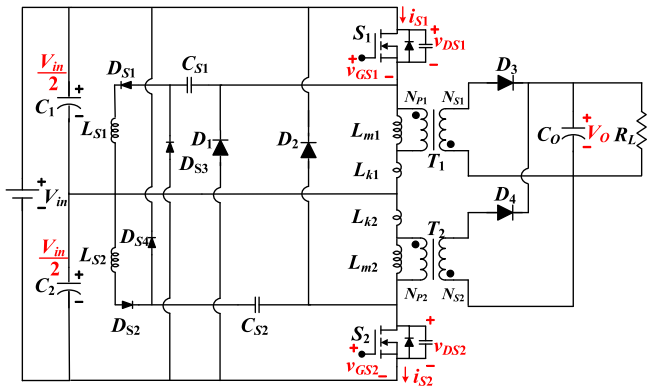

Fig. 2. IHBFC with turn-OFF ZVS [6].

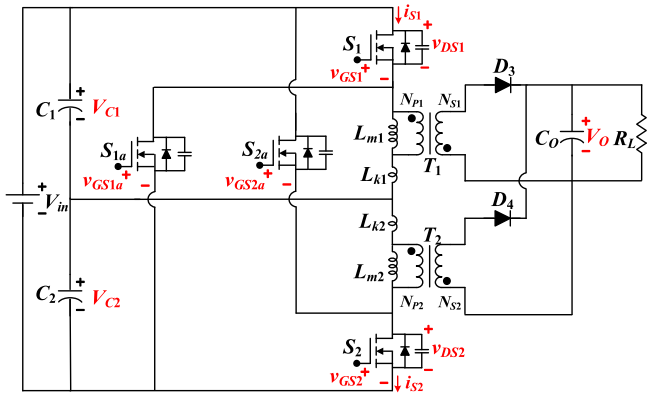

Fig. 3. IHBFC with turn-ON ZVS technology.

The IHBFC with turn-ON ZVS, shown in Fig. 3, can be used to reduce the switch-ON loss by replacing diodes D_1 and D_2 with auxiliary switches S_{1a} and S_{2a}, the key waveforms of which are shown in Fig. 4. The auxiliary switches S_{1a} and S_{2a} are conducted to provide reverse current through the antiparallel diodes of S_1 and S_2. Then, the main switches S_1 and S_2 can achieve turn-ON ZVS at t_2 and t_5, respectively. However, the

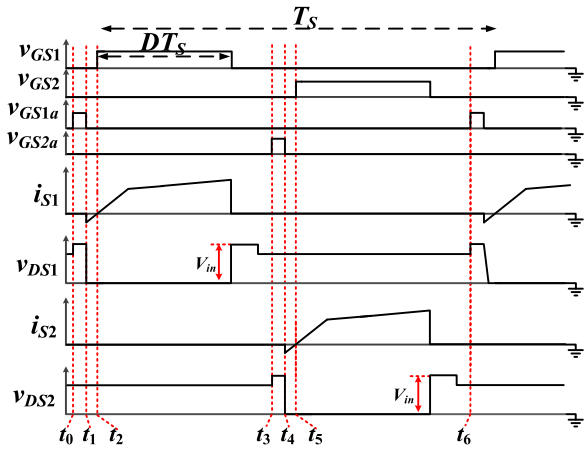

Fig. 4. Key waveforms of the IHBFC with turn-ON ZVS technology.

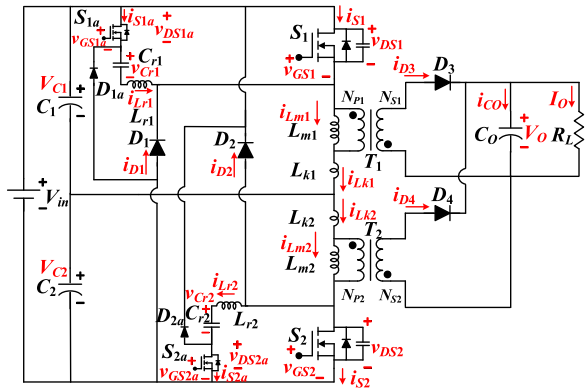

Fig. 5. Proposed IHBFC with turn-OFF ZCS technology.

switching losses of this converter remain very high because the turn-OFF loss dominates the switching losses.

In this paper, a novel IHBFC with ZCS circuits technology to eliminate the switching-OFF loss is proposed, as shown in Fig. 5. With the additional ZCS circuits, the current flowing through the main switches S_1 and S_2 can be transmitted before S_1 and S_2 turn OFF, thereby achieving turn-OFF ZCS under a wide range of operations. In this manner, the efficiency can be improved, with computer simulations verifying the superior performance of this converter compared with [4]–[6].

II. Operating Principle

The proposed topology consists of two flyback converters, Flyback_1 and Flyback_2, as shown in Fig. 5. Capacitors C_1 and C_2, with the same values, are respectively connected to Flyback_1 and Flyback_2, making the two capacitors an input source of the two flyback converters. As a result, the voltage on the primary windings is reduced to half of the input voltage. The circuit of Flyback_1 consists of the capacitor C_1, the main switch S_1, the clamping diode D_1, the transformer T_1, the output rectifier diode D_3, and the resonant branch comprising S_{1a}, D_{1a}, L_{r1}, and C_{r1}; likewise, the circuit of Flyback_2 consists of the capacitor C_2, the main switch S_2, the clamping diode D_2, the transformer T_2, the output rectifier diode D_4, and the resonant

branch comprising S_{2a}, D_{2a}, L_{r2}, and C_{r2}. In order to simplify the steady-state analysis, the following assumptions are made.

1) The leakage inductances in the secondary side of the transformers are referred to the primary side and merged with the leakage inductances in the primary side. L_{k1} and L_{k2} represent the leakage inductances of T_1 and T_2, respectively.
2) The main switches (S_1 and S_2) and the auxiliary switches (S_{1a} and S_{2a}) are ideal.
3) Diodes D_{1a}, D_{2a}, D_1, D_2, D_3, and D_4 are ideal.
4) Transformers T_1 and T_2 are identical, so turns ratio $n = N_{P1}/N_{S1} = N_{P2}/N_{S2}$.
5) Capacitors C_1, C_2, and C_O are large enough for V_{C1}, V_{C2}, and V_O to be constant.
6) The input capacitors C_1=C_2, so $V_{C1} = V_{C2} = V_{\text{in}}/2$.

Fig. 6 shows the key waveforms of the proposed zero-current current-transition (ZCT) converter operated in continuous conduction mode (CCM). As can be seen, one cycle period of the proposed circuit is divided into 16 modes. Modes I–VIII and IX–XVI are the complete operational sections of Flyback_1 and Flyback_2, respectively. The functionality of Flyback_1 and Flyback_2 is the same; similarly, the operation of modes I–VIII is identical to that of modes IX–XVI. Hence, this paper only illustrates how modes I–VIII function. Fig. 7 shows the equivalent ZCT circuits of the operation modes in CCM. Before t_0, all switches are OFF when D_3 and D_4 are conducted. In this condition, the magnetizing inductance current i_{Lm1} releases energy to C_O and R_L through T_1 and D_3; likewise, magnetizing inductance current i_{Lm2} releases energy to C_O and R_L through T_2 and D_4.

Mode I $[t_0, t_1]$: In this interval, v_{GS1} is high, while v_{GS2}, v_{GS1a}, and v_{GS2a} are low. The body diode of S_{1a}, S_1, D_3, and D_4 are ON, whereas S_2, S_{1a}, S_{2a}, D_{1a}, D_{2a}, D_1, and D_2 are OFF. For Flyback_1, C_{r1} and L_{r1} form a half-cycle resonance via S_1 and the body diode of S_{1a}, and make the positive v_{Cr1} turn into negative. In addition, L_{m1} releases energy to L_{k1} and the load simultaneously, i_{Lm1} flows toward C_O and R_L through T_1 and D_3, and i_{D3} decreases rapidly and becomes zero at t_0'. For Flyback_2, i_{Lm2} still flows toward C_O and R_L through T_2 and D_4. When v_{Cr1} reaches the maximum value of the negative voltage at $t = t_1$, mode II begins. The equations of the voltage and current of L_{k1} are described as follows:

$$v_{Lk1}(t) = \frac{1}{2}V_{\text{in}} + nV_o, \text{for } t_0 < t \le t_1 \tag{1}$$

$$\begin{aligned} i_{Lk1}(t) &= \frac{1}{L_{k1}}\int_{t_0}^{t} v_{Lk1}dt + I_{Lk1,t0} \\ &= \frac{1}{L_{k1}}\int_{t_0}^{t}\left(\frac{1}{2}V_{\text{in}} + nV_O\right)dt + I_{Lk1,t0}, \\ &\quad \text{for } t_0 < t \le \ t_1 \end{aligned} \tag{2}$$

i_{D3} can be expressed as follows:

$$i_{D3}(t) = n\left[i_{Lm1}(t) - i_{Lk1}(t)\right], \text{ for } t_0 < t \le \ t_1. \tag{3}$$

Mode II $[t_1, t_2]$: In this interval, v_{GS1} is high, while v_{GS2}, v_{GS1a}, and v_{GS2a} are low; in addition, S_1, D_{1a}, and D_4 are ON whereas S_2, S_{1a}, S_{2a}, D_{2a}, D_1, D_2, and D_3 are OFF. For Flyback_1, L_{r1}, L_{m1}, L_{k1}, and C_2 store the energy released from C_{r1} through D_{1a}, and at the same time, L_{m1}, L_{k1}, and C_2 store the energy released from V_{in}; meanwhile, the energy stored in V_{C1} is released to L_{m1} and L_{k1}. For Flyback_2, i_{Lm2} still flows toward C_O and R_L through T_2 and D_4. The equation for v_{DS1a} is described as follows. When the i_{Lr1} current decays to zero at t_2, mode III begins

$$v_{DS1a}(t) = V_{\text{in}}, \text{ for } t_1 < t \le \ t_2. \tag{4}$$

Mode III $[t_2, t_3]$: In this interval, v_{GS1} is high, while v_{GS2}, v_{GS1a}, and v_{GS2a} are low. S_1 and D_4 are ON, whereas S_2, S_{1a}, S_{2a}, D_{1a}, D_{2a}, D_1, D_2, and D_3 are OFF. For Flyback_1, L_{m1}, L_{k1}, and C_2 store energy released from V_{in}; meanwhile, L_{m1} and L_{k1} store energy released from V_{C1}. In mode III, i_{Lk1} and i_{Lm1} increase linearly, while i_{Lk1} equals i_{Lm1}. For Flyback_2, i_{Lm2} still flows toward C_O and R_L through T_2 and D_4. The

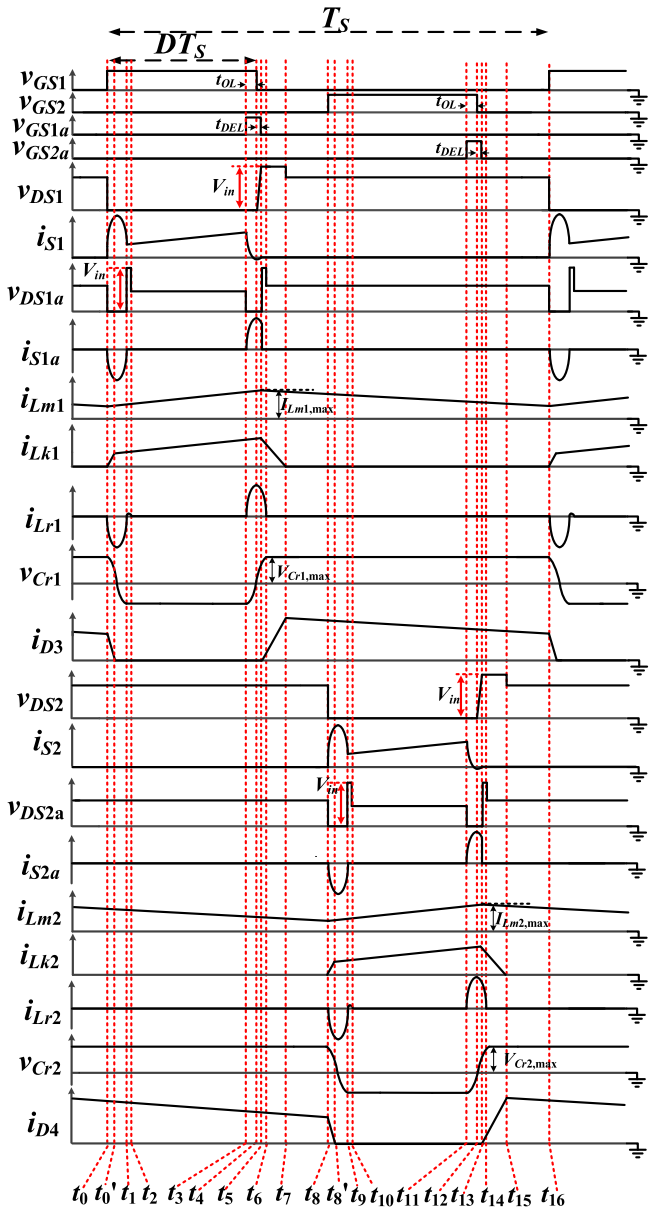

Fig. 6. Key waveforms of the proposed converter with ZCS technology.

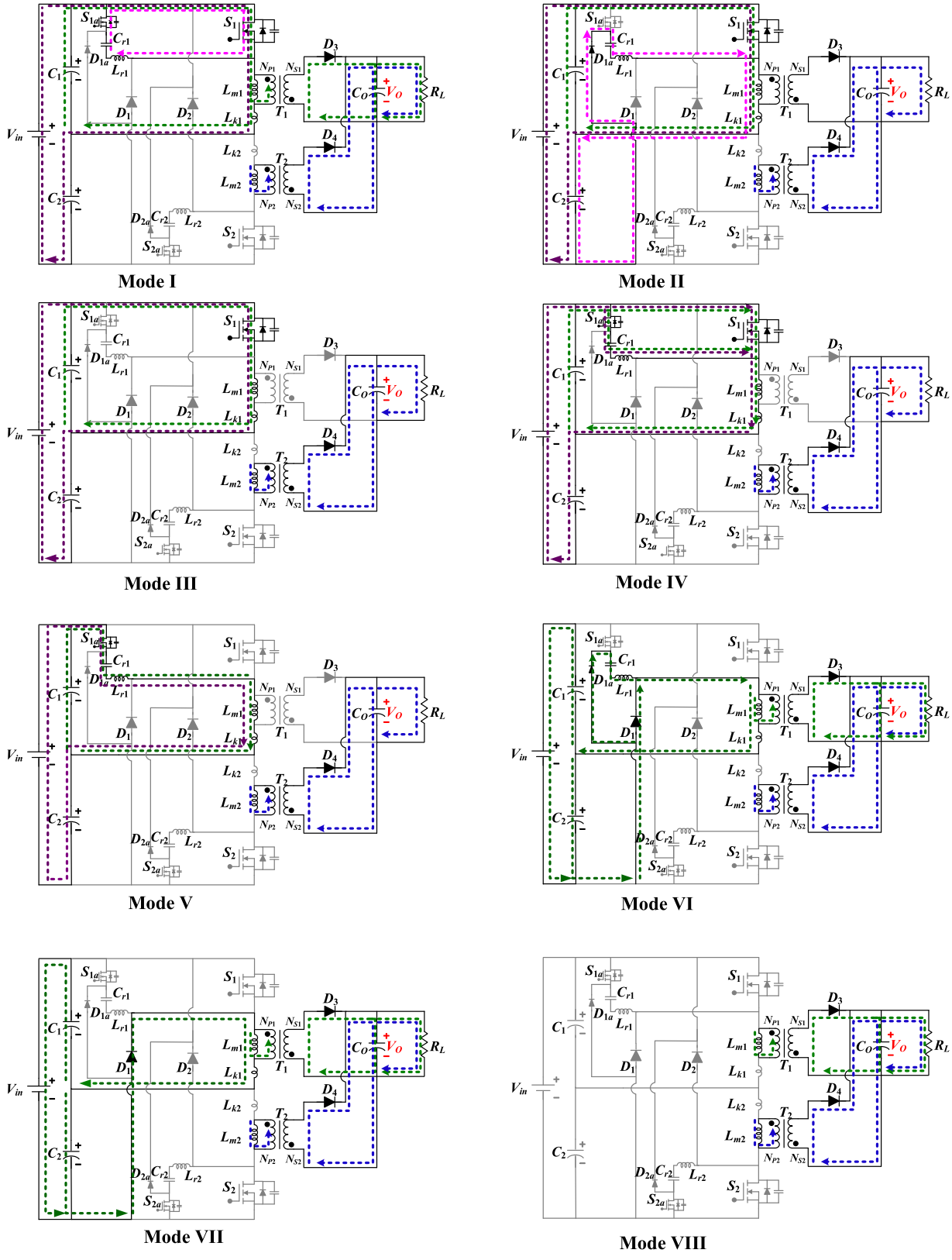

Fig. 7. Equivalent circuits of the operation modes in CCM.

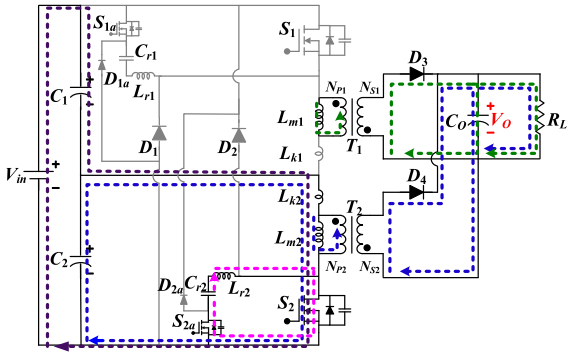

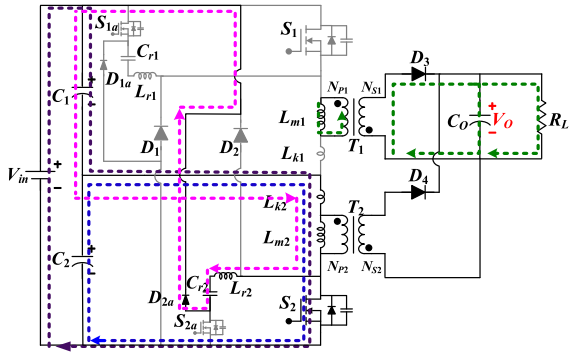

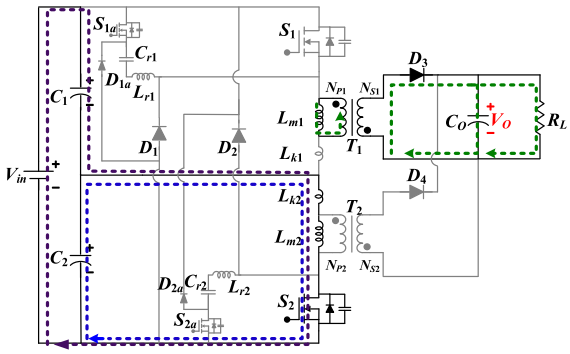

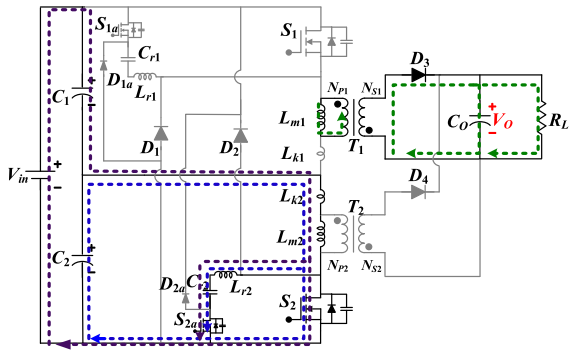

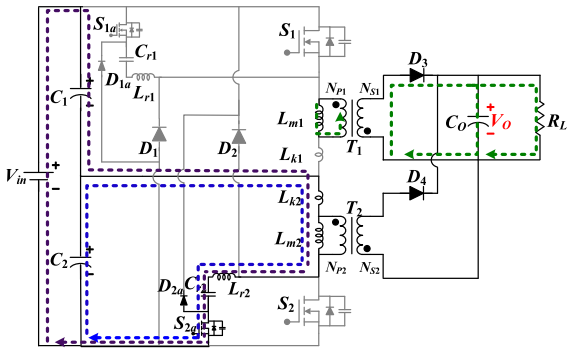

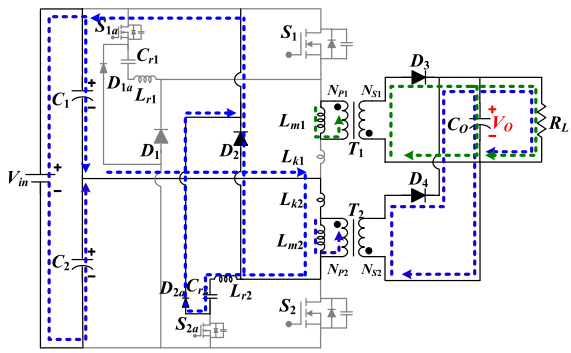

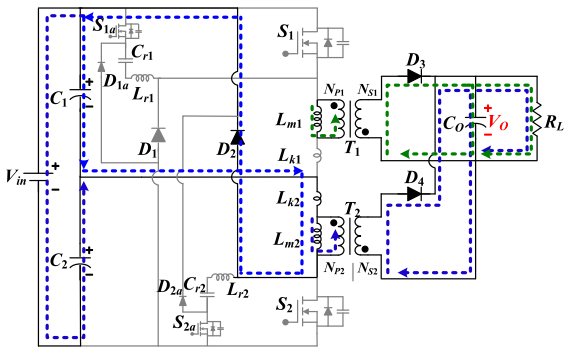

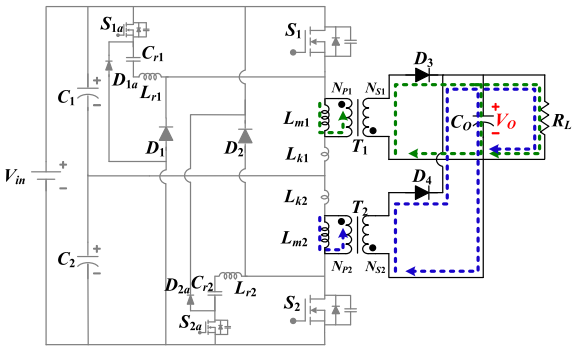

Fig. 7. (Continued).

equations of v_{Lk1} and v_{Lm1} are described as follows. When v_{GS1a} is high, mode IV begins

$$v_{Lk1}(t) = \frac{V_{\text{in}}}{2}\left(\frac{L_{k1}}{L_{m1}+L_{k1}}\right), \text{ for } t_2 < t \leq \ t_3 \quad (5)$$

$$v_{Lm1}(t) = \frac{V_{\text{in}}}{2} - v_{Lk1}(t), \text{ for } t_2 < t \leq \ t_3 \quad (6)$$

i_{Lm1} can be expressed as follows:

$$\begin{aligned} i_{Lm1}(t) &= \frac{1}{L_{m1}}\int_{t_2}^{t} v_{Lm1}dt + I_{Lm1,t2} \\ &= \frac{1}{L_{m1}}\int_{t_2}^{t}\left(\frac{V_{\text{in}}}{2} - v_{Lk1}\right)dt \\ &\quad + I_{Lm1,t2}, \text{ for } t_2 < t \leq \ t_3. \end{aligned} \quad (7)$$

Mode IV $[t_3, t_4]$: In this interval, v_{GS1} and v_{GS1a} are high, while v_{GS2} and v_{GS2a} are low. S_1, S_{1a}, and D_4 are ON, whereas S_2, S_{2a}, D_{1a}, D_{2a}, D_1, D_2, and D_3 are OFF. For Flyback_1, L_{m1}, L_{k1}, and C_2 store energy released from V_{in}; meanwhile, L_{m1} and L_{k1} store energy released from V_{C1}. C_{r1} and L_{r1} start resonance, which makes most of the input current flow to the parallel resonant tank, where Z_r is the impedance of the resonant tank and T_r is the resonant period. t_{OL} is the time period from t_3 to t_4, and at this moment, the two signals v_{GS1} and v_{GS1a} are simultaneously high. If t_{OL} is set as exactly 1/4 of the T_r resonant period, the current i_{S1} would be reduced to zero in the form of a sinusoidal wave at $t = t_4$, and make the transistor's turn-OFF transition occur at zero current. Hence, S_1 achieves ZCS. Meanwhile, the voltage of C_{r1} would decrease to zero and the current of L_{r1} would reach its maximum $I_{Lr1,t4}$, as described in (11). For Flyback_2, i_{Lm2} still flows toward C_O and R_L through T_2 and D_4. When v_{GS1} is low, mode V begins

$$T_r = 2\pi\sqrt{L_{r1}C_{r1}} \quad (8)$$

$$Z_r = \sqrt{L_{r1}/C_{r1}} \quad (9)$$

$$t_{\text{OL}} = \frac{1}{4}T_r \quad (10)$$

$$I_{Lr1,t4} = V_{Cr1,\max}/Z_r \quad (11)$$

i_{S1a} reaches the maximum value at $t = t_4$

$$I_{S1a,\max} = I_{Lr1,t4}. \quad (12)$$

Mode V $[t_4, t_5]$: In this interval, v_{GS1a} is high, while v_{GS1}, v_{GS2}, and v_{GS2a} are low. S_{1a} and D_4 are ON, whereas S_1, S_2, S_{2a}, D_{1a}, D_{2a}, D_1, D_2, and D_3 are OFF. t_{DEL} is the time period from t_4 to t_5 and also the time delay between the v_{GS1} and v_{GS1a} gate-drive turn-OFF signals. For Flyback_1, C_{r1}, L_{r1}, L_{m1}, L_{k1}, and C_2 store energy released from V_{in}; meanwhile, C_{r1}, L_{r1}, L_{m1}, and L_{k1} store energy released from V_{C1}. V_{in} and V_{C1} release energy to C_{r1} via S_{1a} and ensure that the voltage of v_{Cr1} increases continuously. The maximum voltage of v_{Cr1}, $V_{Cr1,\max}$, can be determined by (14), where $I_{Lm1,\max}$ is the peak current of i_{Lm1}. At $t = t_4$, i_{S1} is zero and the current flowing into the resonant inductor L_{r1} approaches equivalence with $I_{Lm1,\max}$. For Flyback_2, L_{m2} releases energy to C_O and R_L via T_2 and D_4. When v_{GS1a} is low, mode VI begins

$$t_{\text{DEL}} = t_5 - t_4 \quad (13)$$

$$V_{Cr1,\max} = \frac{Z_r I_{Lm1,\max}}{\cos(2\pi(t_5-t_4)/T_r)} = \frac{Z_r I_{Lm1,\max}}{\cos(2\pi(t_{\text{DEL}})/T_r)}. \quad (14)$$

Mode VI $[t_5, t_6]$: In this interval, v_{GS1}, v_{GS2}, v_{GS1a}, and v_{GS2a} are low. D_{1a}, D_1, D_3, and D_4 are ON, while S_1, S_2, S_{1a}, S_{2a}, D_{2a}, and D_2 are OFF. For Flyback_1, when S_{1a} turns OFF at t_5, both D_1 and D_{1a} start conducting. The energy of resonant inductance L_{r1} is recycled to C_2 and V_{in} through D_{1a}; meanwhile, the energy of leakage inductance L_{k1} is recycled to C_2 and V_{in} through D_1 directly, and v_{DS1} is clamped at V_{in}. Magnetizing current i_{Lm1} flows toward C_O and R_L through T_1 and D_3; for Flyback_2, i_{Lm2} still flows toward C_O and R_L through T_2 and D_4. When the i_{Lr1} current decays to zero at t_6, mode VII begins. Then, the maximum voltage stress of S_1 and S_{1a} can be derived from the following equations:

$$v_{DS1}(t) = V_{\text{in}}, \text{ for } t_5 < t \leq \ t_7 \quad (15)$$

$$v_{DS1a}(t) = V_{\text{in}}, \text{for } t_5 < t \leq t_6. \quad (16)$$

Mode VII $[t_6, t_7]$: In this interval, v_{GS1}, v_{GS2}, v_{GS1a}, and v_{GS2a} are low. D_1, D_3, and D_4 are ON, while D_{1a}, D_{2a}, D_2, S_1, S_2, S_{1a}, and S_{2a} are OFF. For Flyback_1, the energy of leakage inductance L_{k1} is recycled to C_2 and V_{in} through D_1 directly, and v_{DS1} is clamped at V_{in}. Magnetizing current i_{Lm1} flows toward C_O and R_L through T_1 and D_3; for Flyback_2, i_{Lm2} still flows toward C_O and R_L through T_2 and D_4. When L_{k1} releases all energy and the i_{D1} current decays to zero at t_7, mode VIII begins. The equations for v_{Lm1} and i_{Lm1} are described as follows:

$$v_{Lm1}(t) = -nV_O, \text{ for } t_6 < t \leq t_7 \quad (17)$$

$$\begin{aligned} i_{Lm1}(t) &= \frac{1}{L_{m1}}\int_{t_6}^{t} v_{Lm1}dt + I_{Lm1,t6} \\ &= \frac{1}{L_{m1}}\int_{t_6}^{t}(-nV_O)dt + I_{Lm1,t6}, \text{ for } t_6 < t \leq \ t_7. \end{aligned} \quad (18)$$

The equation for v_{DS1a} is described as follows:

$$v_{DS1a}(t) = V_{Cr1,\max}, \text{ for } t_6 < t \leq \ t_{16}. \quad (19)$$

Mode VIII $[t_7, t_8]$: In this interval, v_{GS1}, v_{GS2}, v_{GS1a}, and v_{GS2a} are low. D_3 and D_4 are ON, while D_{1a}, D_{2a}, D_1, D_2, S_1, S_2, S_{1a}, and S_{2a} are OFF. For Flyback_1, i_{Lm1} flows toward C_O and R_L through T_1 and D_3; for Flyback_2, i_{Lm2} still flows toward C_O and R_L through T_2 and D_4. The equation for v_{DS1} is described as follows:

$$v_{DS1}(t) = \frac{V_{\text{in}}}{2} + nV_O, \text{ for } t_7 < t \leq t_{16}. \quad (20)$$

When $t = t_8$, v_{GS2} is high, mode VIII ends and mode IX begins.

Fig. 8 shows the key waveforms of the proposed converter operating in DCM. As can be seen, one cycle period of the proposed circuit is divided into 16 modes. Modes I–VIII and IX–XVI are

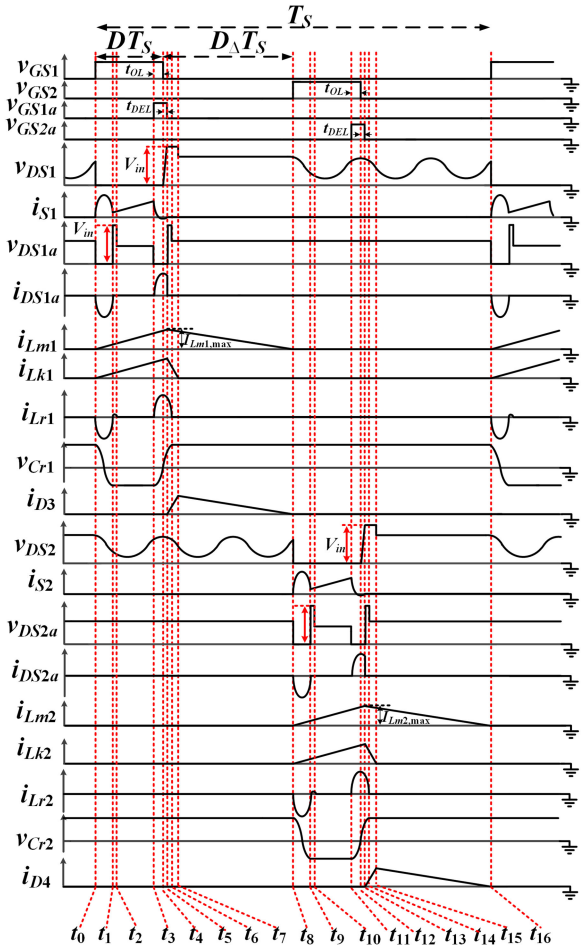

Fig. 8. Key waveforms of proposed converter operated in DCM.

complete operational sections of Flyback_1and Flyback_2, respectively. The functionality of Flyback_1 is the same as that of Flyback_2. Likewise, the operation of modes I–VIII is identical to that of modes IX–XVI. The difference between mode I in DCM and in CCM is that before $t = t_0$, $i_{\mathrm{Lm}1}$ and $i_{\mathrm{D}3}$ have decreased to zero in DCM. Therefore, there is no energy transferred to the secondary side of the transformer via T_1 in mode I. In addition, the difference between modes I–VIII in DCM and CCM is that $i_{\mathrm{Lm}2}$ and $i_{\mathrm{D}4}$ are zero in DCM, which leads to oscillations in the voltage waveforms of $v_{\mathrm{DS}2}$ due to the parasitic capacitor of switch S_2. The magnetizing inductance L_{m2} and the leakage inductance L_{k2} are formed in resonance when i_{Lk2} and i_{Lm2} are equal to zero. The other waveforms are mostly the same.

III. Steady-State Characteristics

A. Relationship Between Input and Output

The proposed topology has two identical flyback converters, which have the same characteristic parameters. Therefore, the circuit parameters of only one flyback converter are analyzed for simplicity.

Since the leakage inductance $L_{k1} << L_{m1}$; $L_{k2} << L_{m2}$, the effect of L_{k1} can be ignored. As a result, the circuit of the proposed converter can be simplified, as depicted in Fig. 9. The

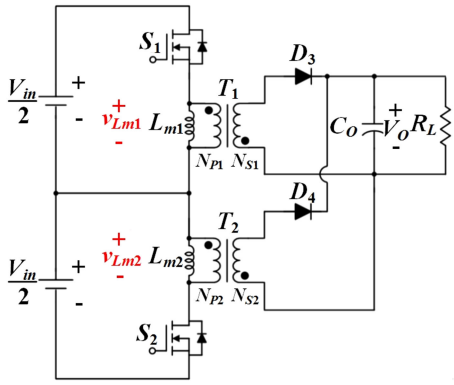

Fig. 9. Simplified circuit of the proposed converter.

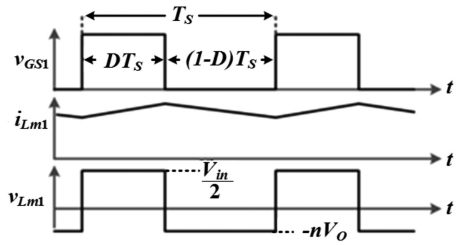

Fig. 10. Waveforms in CCM.

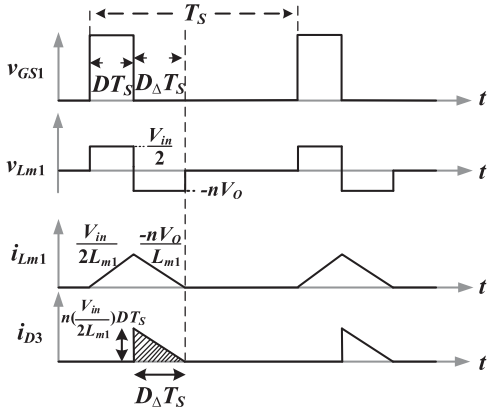

Fig. 11. Waveforms in DCM.

voltage and current waveforms of L_{m1} in CCM and DCM are shown in Figs. 10 and 11, respectively.

Referring to the theoretical waveforms in Fig. 10, the voltages across L_{m1} when the switch is conducting and turned OFF are as follows:

$$v_{Lm1,\mathrm{on}} = \frac{1}{2}V_{\mathrm{in}} \tag{21}$$

$$v_{Lm1,\mathrm{off}} = -\frac{N_{P1}}{N_{S1}}V_O. \tag{22}$$

Using the volt–second balance theory, the following equation can be derived:

$$\frac{1}{2}V_{\mathrm{in}}DT_S = \frac{N_{P1}}{N_{S1}}V_O(1-D)T_S. \tag{23}$$

Recollecting the above equation, the voltage conversion ratio of the proposed converter in CCM is as follows:

$$M_{\mathrm{DC(CCM)}} = \frac{V_O}{V_{\mathrm{in}}} = \frac{1}{2}\frac{N_{S1}}{N_{P1}}\frac{D}{1-D} = \frac{1}{2}\frac{D}{n(1-D)}. \quad (24)$$

Fig. 11 shows the waveforms of the flyback converter in DCM, for which the voltages across L_{m1} during ON and OFF periods are as follows:

$$v_{Lm1,\mathrm{on}} = \frac{1}{2}V_{\mathrm{in}} \quad (25)$$

$$v_{Lm1,\mathrm{off}} = -\frac{N_{P1}}{N_{S1}}V_O. \quad (26)$$

Using the volt–second balance theory of L_{m1}, we have

$$\frac{1}{2}V_{\mathrm{in}}DT_S = \frac{N_{P1}}{N_{S1}}V_O D_\Delta T_S. \quad (27)$$

The voltage conversion ratio of the proposed converter in DCM is

$$M_{\mathrm{DC(DCM)}} = \frac{V_O}{V_{\mathrm{in}}} = \frac{1}{2}\frac{D}{nD_\Delta} \quad (28)$$

where $D_\Delta T_S$ is defined as the time interval when L_{m1} releases energy to the output. The average output current can be expressed as follows:

$$I_O = \frac{V_O}{R_L} = \frac{1}{T_S}\int_0^{T_S} i_{D3} + i_{D4}dt = \frac{2}{T_S}\int_{DT_S}^{(D+D_\Delta)T_S} i_{D3}dt \quad (29)$$

$i_{D3} = ni_{Lm1}$ during the time when L_{m1} releases energy to the output. From Fig. 11, the area of i_{D3} can be determined via general equation of triangle area. Therefore, (29) can be rewritten as follows:

$$I_O = \frac{2}{T_S}\int_{DT_S}^{(D+D_\Delta)T_S} i_{D3}dt = \frac{2}{T_S} \times \frac{n\left(\frac{V_{\mathrm{in}}}{2L_{m1}}\right)DT_S \times D_\Delta T_S}{2} = \frac{V_O}{R_L}. \quad (30)$$

From (28) and (30), voltage gain can be modified as follows:

$$M_{\mathrm{DC(DCM)}} = \frac{V_O}{V_{\mathrm{in}}} = \frac{1}{2}\frac{D}{nD_\Delta} = \frac{nDD_\Delta T_S R_L}{2L_{m1}}. \quad (31)$$

The duty ratio of L_{m1} releasing energy to the output, D_Δ, can be derived as follows:

$$D_\Delta = \sqrt{\frac{L_{m1}}{n^2 T_S R_L}} = \sqrt{\frac{L_{m1}I_O}{n^2 T_S V_O}} \quad (32)$$

Then, voltage gain shown in (28) can be modified as

$$M_{\mathrm{DC(DCM)}} = \frac{D}{2nD_\Delta} = \frac{D}{2\sqrt{\frac{L_{m1}}{T_S R_L}}} = \frac{D}{2\sqrt{\frac{L_{m1}I_O}{T_S V_O}}}. \quad (33)$$

B. ZCS Condition

From Fig. 6, during t_3 to t_4, and according to the KCL rule

$$i_{Lm1}(t) = i_{Lr1}(t) + i_{S1}(t). \quad (34)$$

To achieve ZCT, the current flowing through power switch S_1 should be less than zero at $t = t_4$. Therefore, the ZCS condition can be described as follows:

$$I_{Lr1,t4} \geq I_{Lm1,t4}. \quad (35)$$

Because t_{DEL} is very small, $I_{Lm1,t4}$ is almost equal to $I_{Lm1,\max}$; therefore, the ZCS condition can be rewritten as (37)

$$I_{Lm1,t4} \cong I_{Lm1,\max} \quad (36)$$

$$I_{Lr1,t4} \geq I_{Lm1,\max}. \quad (37)$$

By integrating (11) and (14) with (37), the following expression can be derived:

$$\cos(2\pi(t_{\mathrm{DEL}})/T_r) \leq 1. \quad (38)$$

Equation (38) indicates that as long as t_{DEL} is smaller than T_r, $I_{Lr1,t4}$ will always be larger than or equal to $I_{Lm1,\max}$. Another restriction is that $V_{Cr1,\max}$ cannot be higher than V_{in} in a steady-state operational period; otherwise, the body diode of S_1 would conduct during the $t_2 - t_3$ period. Therefore, $V_{Cr1,\max}$ must comply with the following equation:

$$V_{Cr1,\max} \leq V_{\mathrm{in}}. \quad (39)$$

By integrating (14) with (39), the following inequality can be derived, to which t_{DEL} must comply

$$t_{\mathrm{DEL}} < T_r \times \frac{\cos^{-1}\left(\frac{Z_r I_{Lm1,\max}}{V_{in}}\right)}{2\pi} \quad (40)$$

where $I_{Lm1,\max}$ can be shown in the following equation, $I_{Lm1,\mathrm{avg}}$ is the average value of i_{Lm1}, ΔI_{Lm1} is the peak-to-peak value of the ripple current through the magnetizing inductance L_{m1}:

$$I_{Lm1,\max} = I_{Lm1,\mathrm{avg}} + \frac{1}{2}\Delta I_{Lm1} = \frac{I_O}{2n(1-D)} + \frac{nV_O(1-D)T_S}{2L_{m1}} = \frac{L_{m1}I_O + n^2(1-D)^2 V_O T_S}{2n(1-D)L_{m1}}. \quad (41)$$

In practice, t_{DEL} can be set as $0.1T_r$, in which case $I_{Lr1,t4}$ would be equal to about 1.2 times $I_{Lm1,\max}$, and so ZCS could easily be achieved. The duty ratio of auxiliary switch D_a is described in the following equation. In addition, based on (10), $t_{\mathrm{OL}} = 0.25T_r$; therefore,

$$D_a = (0.35\,T_r)/T_S$$

$$D_a = \frac{t_{\mathrm{OL}} + t_{\mathrm{DEL}}}{T_S} \quad (42)$$

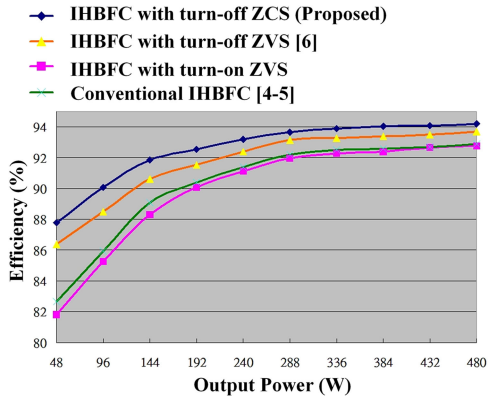

Fig. 12. Efficiency comparison of IHBFCs [4]–[6].

C. Design of the Magnetic Element

The number of turns on the primary (N_{P1}, N_{P2}) and secondary (N_{S1}, N_{S2}) sides of the transformer can be determined by the following equations:

$$N_{P1} = N_{P2} = \frac{I_{Lm1,\max} L_{m1}}{A_{\text{eff}} \Delta B} = \frac{I_{Lm2,\max} L_{m2}}{A_{\text{eff}} \Delta B} \tag{43}$$

$$N_{S1} = N_{S2} = \frac{N_{P1}}{n} = \frac{N_{P2}}{n} \tag{44}$$

$$n = \frac{N_{P1}}{N_{S1}} = \frac{N_{P2}}{N_{S2}} = \frac{D_{\max} V_{\text{in}}}{2\left(1 - D_{\max}\right) V_O} \tag{45}$$

where ΔB is the flux density and normally 0.7 times the value of the saturating flux density, A_{eff} is the effective area of the core, and $D_{\max}$ is the maximum duty ratio of the main switch. The BCM of the converter is designated to be 40% of the rated output power. Hence, the boundary output power of each converter is

$$P_{B,\text{Single}} = \frac{1}{2} \times 0.4 \times P_O. \tag{46}$$

Based on the energy equation of the inductor, the boundary output power of each converter can be expressed as

$$P_{B,\text{Single}} = \frac{\frac{L_{m1} \Delta I_{Lm1,BCM}^2}{2}}{T_S} = \frac{f_S L_{m1} \Delta I_{Lm1,BCM}^2}{2} = \frac{f_S L_{m1} \left(\frac{n V_O \left(1 - D_{\max}\right) T_S}{L_{m1}}\right)^2}{2} \tag{47}$$

where $\Delta I_{Lm1,BCM}$ is the value of ΔI_{Lm1} at the BCM. Then, L_{m1} and L_{m2} can be derived as

$$L_{m1} = \frac{\left(1 - D_{\max}\right)^2 n^2 V_O^2}{2 P_{B,\text{Single}} f_S}. \tag{48}$$

IV. Simulation and Experimental Results

Four topologies, a conventional IHBFC [4], [5], an IHBFC with turn-OFF ZVS [6], an IHBFC with turn-ON ZVS, and the proposed IHBFC with turn-OFF ZCS were simulated under the same specifications. The simulated results shown in Fig. 12 reveal that the proposed IHBFC with turn-OFF ZCS has the highest efficiency among the compared topologies due to the turn-OFF switching loss playing an important role at the higher switching frequency. Because the proposed converter uses active turn-OFF ZCS, the efficiency is higher than the passive turn-OFF ZVS IHBFC proposed in [6].

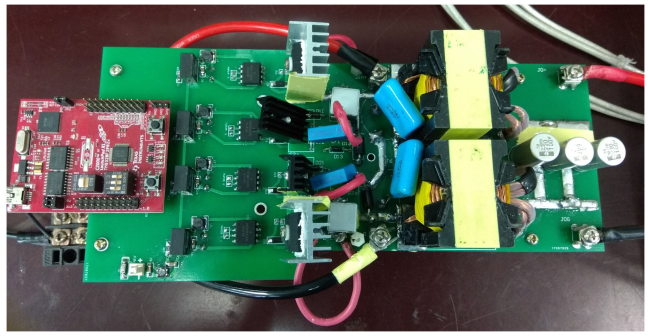

Fig. 13. Experimental prototype.

TABLE I
Key Parameters of the Proposed Circuit

System Specifications	
Input voltage	**400 V**
Output voltage	**24 V**
Maximum output power	**480 W**
Operating frequency	**100 kHz**
Components	**Parameters**
S_1, S_2	IRFP460 (500V/20A)
S_{1a}, S_{2a}	TK7A60W (600V/7A)
D_{1a}, D_{2a}	ER106 (600V/1A)
D_1, D_2	MUR460 (600V/4A)
D_3, D_4	MBR20200CTG (200V/20A)
$N_{P1}/N_{S1} = N_{P2}/N_{S2}$	5.4 (turns ratio)
L_{m1}, L_{m2}	334 μH
L_{k1}, L_{k2}	12 μH
L_{r1}, L_{r2}	5 μH
C_{r1}, C_{r2}	8.2 nF
C_1, C_2	470 μF
C_O	660 μF

A 480-W experimental prototype is implemented to verify the performance of the proposed converter, as shown in Fig. 13. The system specifications and components are listed in Table I. The proposed ZCT converter has two resonant branches, which a conventional converter lacks. In Flyback_1, D_{1a}, S_{1a}, L_{r1}, and C_{r1} are added; in Flyback_2, D_{2a}, S_{2a}, L_{r2}, and C_{r2} are added. Since the auxiliary switches only conduct for a very short period of time, the average current flowing through the auxiliary switches is very small. Therefore, the

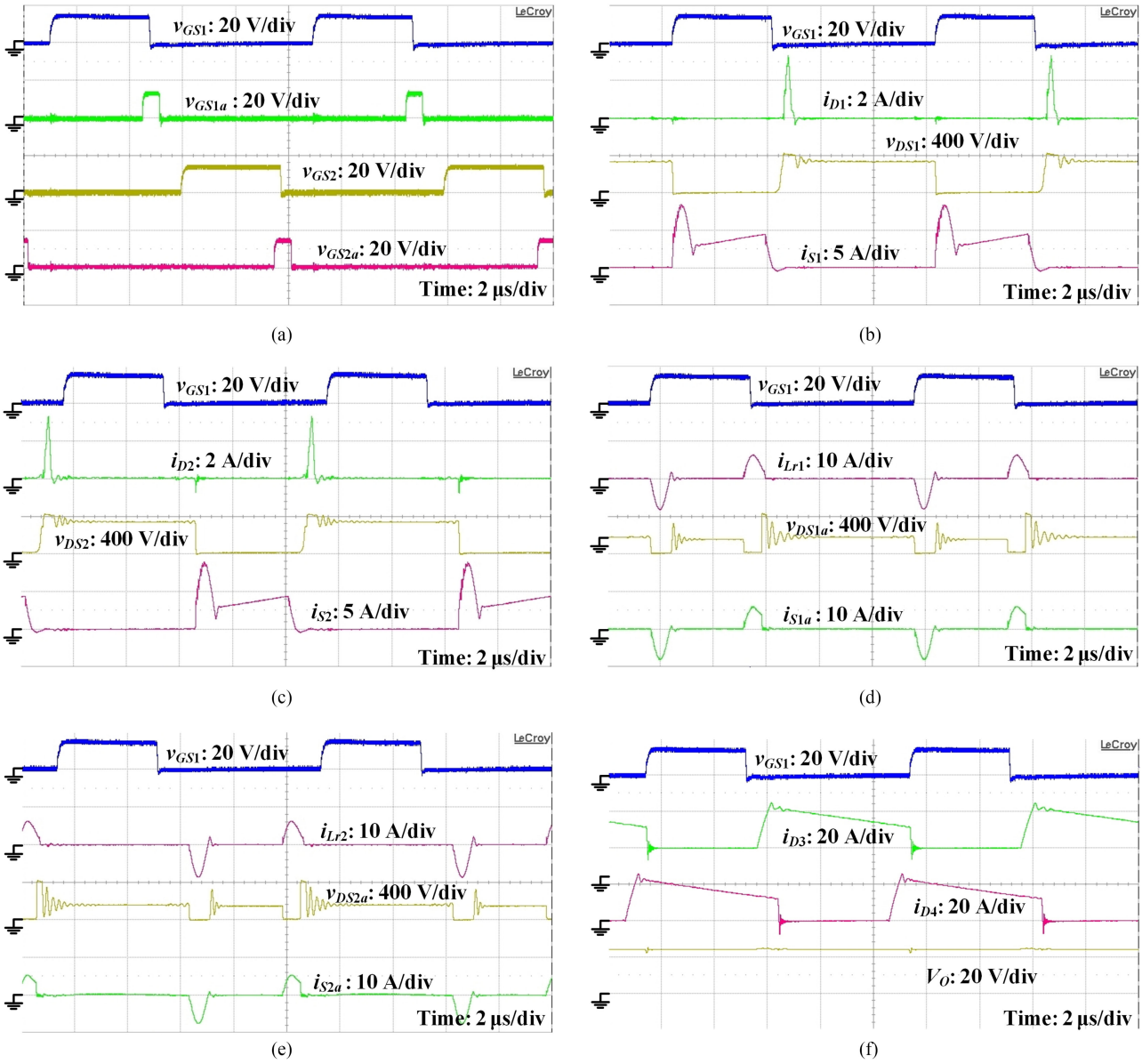

Fig. 14. Measured waveforms at $P_O = 480$ W and $V_O = 24$ V.

switch with the lower-rated current is used as the auxiliary switch.

The key waveforms of the experimental results at full load are shown in Fig. 14. According to Fig. 14(a), S_1 and S_2 are operated interleavely, and S_{1a} and S_{2a} are turned ON for a short period immediately before S_1 and S_2 are turned OFF. Then, the current flowing through the main switches S_1 and S_2 can be transmitted before they are turned OFF to achieve turn-OFF ZCS. Fig. 14(b) shows the waveforms of v_{GS1}, i_{D1}, v_{DS1}, and i_{S1}, while Fig. 14(c) shows the waveforms of v_{GS1}, i_{D2}, v_{DS2}, and i_{S2}. These figures verify that the main switches S_1 and S_2 can achieve ZCS, and the energy stored in L_{k1} and L_{k2} can be recycled to C_2 and V_{in} through D_1 and D_2, respectively. Consequently, the voltage stresses of S_1 and S_2 are clamped at the value of V_{in}. Fig. 14(d) shows the waveforms of v_{GS1}, i_{Lr1}, v_{GS1a}, and i_{S1a}. Fig. 14(e) shows the waveforms of v_{GS1}, i_{Lr2}, v_{DS2a}, and i_{S2a}. These figures reveal that the maximum voltages on the auxiliary switches are clamped at the dc input voltage. Fig. 14(f) shows the waveforms of v_{GS1}, i_{D3}, i_{D4}, and V_O, in which the value of current i_{D3} is almost equal to current i_{D4} with 180 degrees out of phase, and the output current ripple can be reduced. Fig. 15(a)–(f) shows the experimental results at 20% load, with the converter operated in DCM. These figures also demonstrate that the proposed converter can achieve turn-OFF ZCS, leakage energy recycling, and voltage clamping on the power switches.

Fig. 16 presents an efficiency comparison of the proposed converter and a conventional IHBFC. As can be seen, the efficiency of the proposed converter can achieve 93.05% at full load, compared with 91.88% for the conventional IHBFC

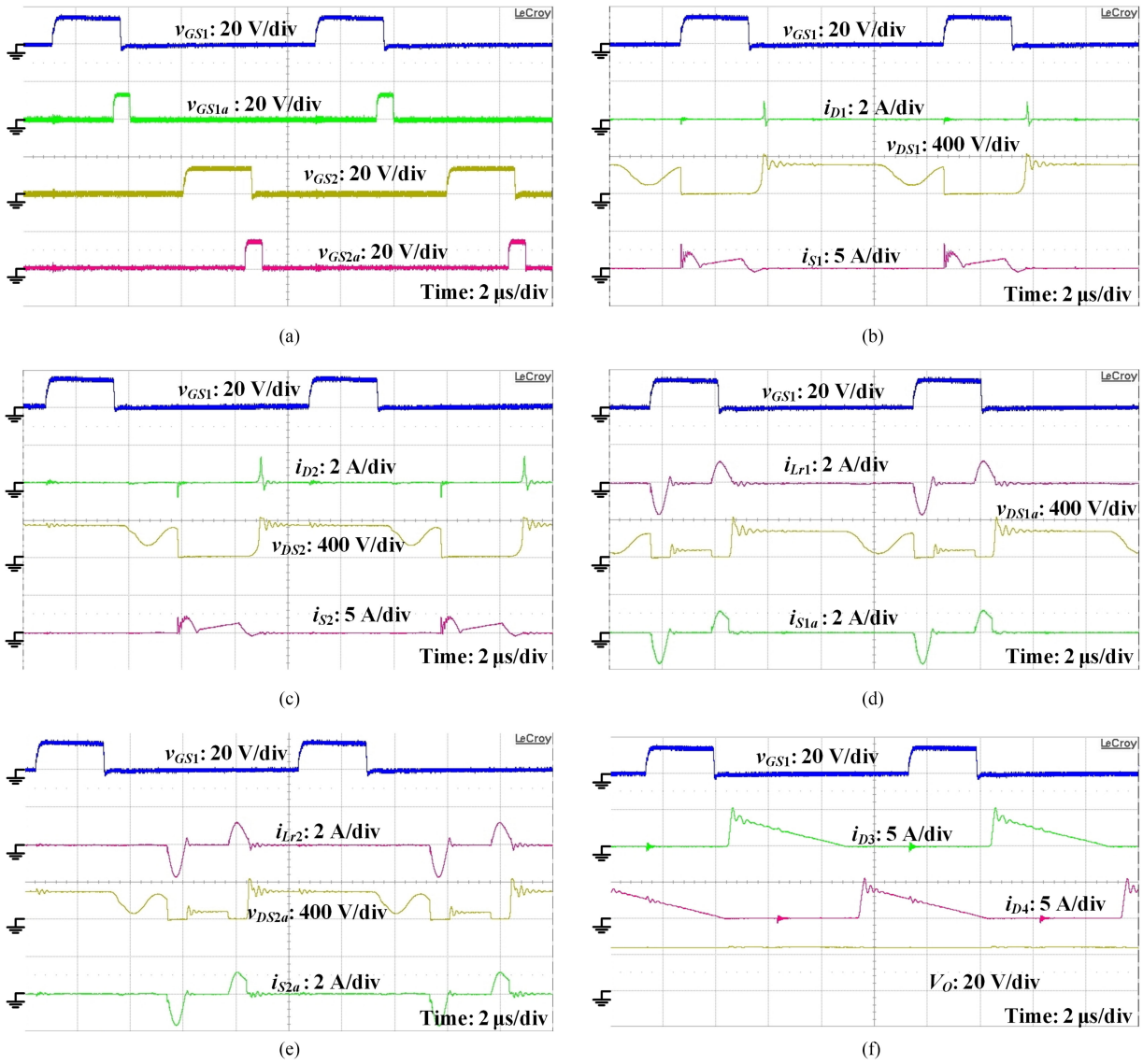

Fig. 15. Measured waveforms at $P_O = 96$ W and $V_O = 24$ V.

under the same condition. Table II shows a comparison of the measured losses for a conventional IHBFC [4], [5] and the proposed IHBFC with turn-OFF ZCS operated at 400 V input and 480 W output. For the conventional IHBFC, the turn-OFF losses of the main switches are about 9.96 W; however, after applying ZCT technology, the turn-OFF losses of the main switches drop to 0.7 W. In addition, the losses of the auxiliary switches and parallel resonant network are approximately 2.59 W together, which is less than 0.6% of the output power.

A 480-W experimental prototype is implemented to verify the performance of the proposed converter with a TI TMS320F28027 controller for realizing PI control, as shown in Fig. 17. Parameters k_p and k_i are 0.9 and 0.01, respectively. The dynamic behavior of the control system is shown in Fig. 18. Fig. 18(a) and (b) presents the variations of output voltage V_O with I_O varied from 4 to 20 A and from 20 to 4 A, respectively.

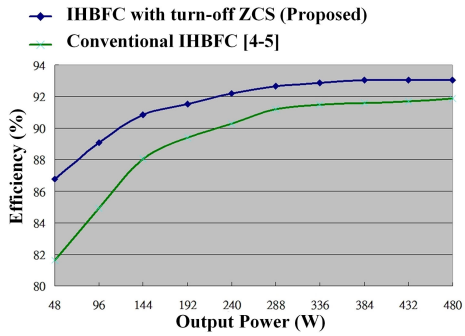

Fig. 16. Efficiency of the proposed converter compared with a conventional IHBFC [4], [5].

It takes about 0.8 ms for V_O to return to a steady 24 V, and the maximum transient swing voltage is less than 0.7 V when I_O is changed from 4 to 20 A. Furthermore, it takes about 0.9 ms

TABLE II
POWER LOSS ANALYSIS FOR TWO IHBFCS AT $V_{IN} = 400$ V

Component losses	Interleaved half-bridge flyback[4-5]	Proposed ZCT-Interleaved half-bridge flyback
Main switches conduction	1.71W	1.8 W
Main switches turn-on	2.6 W	2.6 W
Main switches turn-off	9.96 W	0.7 W
Auxiliary switches	0 W	1.8 W
Auxiliary diodes	0 W	0.49 W
Resonant network	0 W	0.3 W
Clamping diodes	1.65 W	1.65 W
Transformers	7.8 W	7.8 W
Rectifier diodes	16.24 W	16.24 W
Others	2.47 W	2.47 W
Total	42.43 W	35.85 W
Efficiency	91.88 %	93.05 %

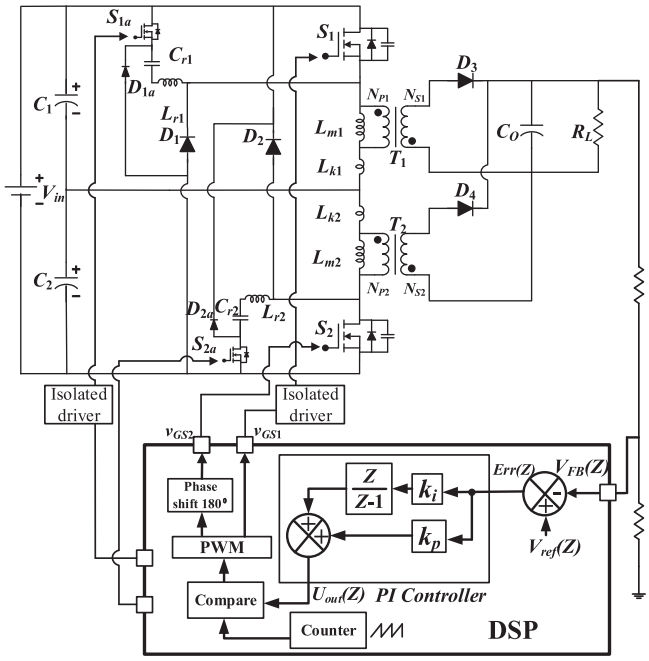

Fig. 17. Block diagram of the control system.

for V_O to return to a steady 24 V, with the maximum transient swing voltage being less than 0.6 V when I_O is changed from 20 to 4 A.

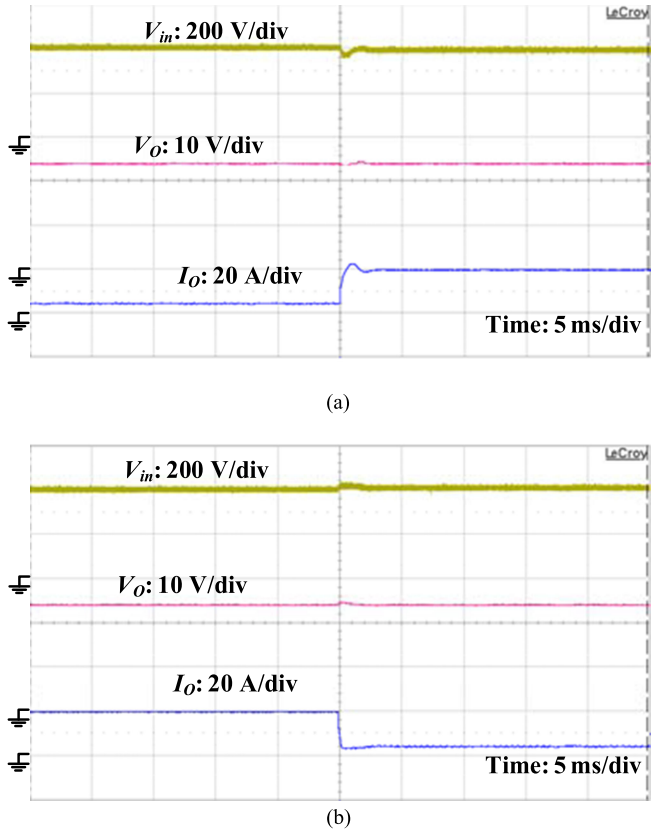

Fig. 18. Dynamic behavior of the control system. (a) I_O is changed from 4 to 20 A. (b) I_O is changed from 20 to 4 A.

V. CONCLUSION AND FUTURE WORK

This paper proposed a novel IHBFC combined with leakage energy recycling and ZCT technology and elaborated the operating principles and characteristics of the circuits. The circuit was verified to achieve high efficiency through an experimental prototype. The primary feature of the proposed circuit structure is reducing the input voltage of the converter by connecting capacitors C_1 and C_2 in series. In doing so, the transformer can function in smaller turns ratio, the leakage inductance of the transformer can be reduced, and the coupling of the energy-storage transformer can be improved. The leakage energy is directly recycled through the clamping diodes, and the voltage across the switches are clamped at V_{in}. The two flyback converters apply interleaved operation so as to reduce output current ripple. The major switching losses of the IHBFC are the turn-OFF losses. To reduce those losses, the proposed circuit ensures the main switches achieve ZCS and reduce the turn-OFF losses by applying auxiliary switches and parallel resonant networks.

Based on the parallel resonant networks, this paper proposed a novel ZCT IHBFC that provides a zero-current turn-OFF function and retains the benefits of an IHBFC; for example, the main switch can hold low-voltage stresses and apply constant-frequency operations. Since the parallel resonant networks and auxiliary switches only operate during switching-transition, the

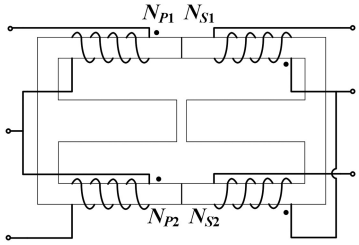

Fig. 19. Integrated transformer for an interleaved flyback converter.

operation methods of the proposed converter are the same as those of a pulsewidth modulation converter in the major switching period. Therefore, the design and control of power devices are similar to those of a conventional IHBFC. In addition, the ZCT operation is independent of the line voltage and load condition, and the circulating energy can maintain a minimum value. These benefits make the proposed converter advantageous in high-power applications. Based on the measured data of the implemented circuit at full load, the proposed circuit structure achieves the efficiency of 1.17% higher than a conventional IHBFC for less switching losses, and improves the efficiency by 4.12% higher than a conventional converter at 20% load. The highest efficiency is 93.06% at 90% load and 93.05% at full load.

Future works to improve the performance of the proposed converter are outlined in the following.

1) The proposed ZCS interleaved converter suffers from the power imbalance problem due to parameter variations. Accordingly, it is suggested to study current-sharing control/power-sharing control to alleviate this issue.
2) The transformer could be improved in following ways. Since the first and second sets of flyback converter are operated in an interleaved manner, transformers T_1 and T_2 would neither generate alternating currents flowing through the primary windings nor further generate magnetic flux to cut the secondary windings during the same time period. In addition, rectifying diodes D_3 and D_4 restrain the direction of the output current in the secondary windings. As a result, transformers T_1 and T_2 could actually apply the same core, as shown in Fig. 19. Since T_1 and T_2 apply the same core, the cost and size of the circuit could be reduced.

REFERENCES

[1] C. Wang, S. Xu, and W. Sun, "An accurate design method of RCD circuit for flyback converter considering diode reverse recovery," in *Proc. IEEE ICIT Conf.* , May 2016, pp. 269–274.
[2] J. Umuhoza, Y. Zhang, and Y. Liu, "Interleaved flyback based microinverter for residential photovoltaic application in remote areas," in *Proc. IEEE 16th Workshop Control Model. Power Electron.*, Jul. 2015, pp. 1–6.
[3] R. J. Wai and B. H. Chen, "High-efficiency dual-input interleaved DC–DC converter for reversible power sources," *IEEE Trans. Power Electron.*, vol. 29, no. 6, pp. 2903–2921, Jun. 2014.
[4] C. H. Wu *et al.*, "Design and implementation of a novel interleaved flyback converter with leakage energy recycled," in *Proc. IEEE Energy Convers. Congr. Expo.*, 2015, pp. 5888–5895.
[5] J. W. Kim, I. O. Lee, and G. W. Moon, "Series input parallel output interleaved flyback converter with regenerative leakage inductance energy," in *Proc. 7th IEEE Int. Power Electron. Motion Control Conf.*, 2012, pp. 1347–1352.
[6] M. Mohammadi and E. Adib, "Lossless passive snubber for half bridge interleaved flyback converter," *IET Power Electron.*, vol. 7, pp. 1475–1481, Jun. 2014.
[7] F. Forest, B. Gelis, and J. J. Huselstein, "Design of a 28 V-to-300 V/12 kW multicell interleaved flyback converter using intercell transformers," *IEEE Trans. Power Electron.*, vol. 25, no. 8, pp. 1966–1974, Feb. 2010.
[8] F. Forest, E. Laboure, and T. A. Meynard, "Multicell interleaved flyback using intercell transformers," *IEEE Trans. Power Electron.*, vol. 22, no. 5, pp. 1662–1671, Sep. 2007.
[9] C. Chang and M. A. Knights, "Interleaving technique in distributed power conversion system," *IEEE Trans. Circuit Syst. I, Fundam. Theory Appl.*, vol. 42, no. 5, pp. 245–251, May 1995.
[10] A. Thangavelu, V. Senthilkumar, and D. Parvathyshankar, "Zero voltage switching-pulse width modulation technique-based interleaved flyback converter for remote power solutions," *IET Power Electron.*, vol. 9, pp. 1381–1390, Jun. 2016.
[11] W. Li, J. Shi, M. Hu, and X. He, "An isolated interleaved active-clamp ZVT flyback-boost converter with coupled inductors," in *Proc. IEEE Power Electron. Appl. Conf.*, 2007, pp. 1–9.
[12] Y. K. Lo and J. Y. Lin, "Active-clamping ZVS flyback converter employing two transformers," *IEEE Trans. Power Electron.*, vol. 22, no. 6, pp. 2416–2423, Nov. 2007.
[13] H. L. Cheng, Y. N. Chang, H. C. Yen, C. C. Hua, and P. Y. Su, "A novel interleaved flyback-typed converter with ZVS operation," in *Proc. IEEE Power Electron. Conf.*, 2016, pp. 1–6.
[14] W. Li and X. He, "Inherent clamp flyback–buck converter with winding cross-coupled inductors," *IET Power Electron.*, vol. 4, no. 1, pp. 111–121, 2011.
[15] J. Zhao, H. Zhao, and F. Dai, "A novel ZVS PWM interleaved flyback converter," in *Proc. 2nd IEEE Conf. Ind. Electron. Appl.*, 2007, pp. 337–341.
[16] Y. C. Hsieh, M. R. Chen, and H.-L. Cheng, "An interleaved flyback converter featured with zero-voltage transition," *IEEE Trans. Power Electron.*, vol. 26, no. 1, pp. 79–84, Jan. 2011.
[17] K. Soltanzadeh, H. Khalilian, and M. Dehghani, "Analysis, design and implementation of a zero voltage switching two-switch CCM flyback converter," *IET Circuits, Dev. Syst.*, vol. 10, pp. 20–28, Jan. 2016.
[18] N. T. Quang, H. J. Chiu, and Y. K. Lo, "Zero-voltage switching current-fed flyback converter for power factor correction application," *IET Power Electron.*, vol. 7, pp. 1971–1978, Nov. 2013.
[19] Z. Zhang, M. Chen, and W. Chen, "Analysis and implementation of phase synchronization control strategies for BCM interleaved flyback microinverters," *IEEE Trans. Power Electron.*, vol. 29, no. 11, pp. 5921–5932, Jan. 2014.
[20] M. Mohammadi, E. Adib, and H. Farzanehfard, "Lossless passive snubber for double ended flyback converter with passive clamp circuit," *IET Power Electron.*, vol. 7, pp. 245–250, Feb. 2014.
[21] M. A. Rezaei, K. J. Lee, and A. Q. Huang, "A high-efficiency flyback micro-inverter with a new adaptive snubber for photovoltaic applications," *IEEE Trans. Power Electron.*, vol. 31, no. 1, pp. 318–327, Mar. 2016.
[22] J. Y. Lee, G. W. Moon, H. J. Park, and M. J. Youn, "Integrated ZCS quasi-resonant power factor correction converter based on flyback topology," *IEEE Trans. Power Electron.*, vol. 15, no. 4, pp. 634–643, Jul. 2000.
[23] F. C. Lee, "High-frequency quasi-resonant converter technologies," *Proc. IEEE*, vol. 76, no. 4, pp. 377–390, Apr. 1988.
[24] M. Forouzesh, K. Yari, and A. Baghramian, "Single-switch high step-up converter based on coupled inductor and switched capacitor techniques with quasi-resonant operation," *IET Power Electron.*, vol. 10, pp. 240–250, Feb. 2017.
[25] Z. Fang, T. Cai, S. Duan, and C. Chen, "Optimal design methodology for LLC resonant converter in battery charging applications based on time-weighted average efficiency," *IEEE Trans. Power Electron.*, vol. 30, no. 10, pp. 5469–5483, Oct. 2015.
[26] C. C. Hua, Y. H. Fang, and C. W. Lin, "LLC resonant converter for electric vehicle battery chargers," *IET Power Electron.*, vol. 7, pp. 2369–2376, Oct. 2014.

Tsorng-Juu Liang (M'93–SM'10–F'16) received the M.S. and Ph.D. degrees in electrical engineering from the University of Missouri, Columbia, MI, USA, in 1990 and 1993, respectively.

He is currently a Distinguished Professor with National Cheng Kung University (NCKU), Tainan, Taiwan, R.O.C. Currently, he serves as an Associate Dean of the College of Electrical Engineering and Computer Science as well as the Director of Green Energy Electronics Research Center, NCKU. He has authored or coauthored 73 journals, more than 170 conference papers, and 32 patents. His research interests include power IC design, high-efficiency power converters, high-efficiency lighting systems, and renewable energy conversion.

Dr. Liang received the Outstanding Professor Award from Chinese Institute of Engineering in 2015. He is the Associate Editor of IEEE TRANSACTIONS ON POWER ELECTRONICS, the BoG of Taiwan Power Electronics Association, and the BoG of The Chinese Institute of Electrical Engineering, Kaohsiung Branch. From 2014 to 2015, he was the Distinguished Lecturer of IEEE Circuits and Systems Society. He was the Board of Directors for Catcher Technology, Compucase Enterprise, EpiLED, and Leadtrend Technology, and the Chair of IEEE Tainan Section and the Technical Committee TC6 Chair of IEEE Power Electronics Society. He also served as the Organizing Committee Member of IEEE International Future Energy Electronics Conference in 2013 and 2015, and the General Chair of IFEEC2017-ECCE Asia.

Ming-Hsien Cheng was born in Taichung, Taiwan, R.O.C., in 1977. He received the B.S. and degrees in electrical engineering from I-Shou University, Kaohsiung, Taiwan, R.O.C., and National Cheng Kung University (NCKU), Tainan, Taiwan, R.O.C., in 2003 and 2005, respectively. He is currently working toward the Ph.D. degree at NCKU.

His research interests include high-efficiency power converters, ultrasonic motor drivers, radio frequency plasma power supplies, and uninterruptible power systems.

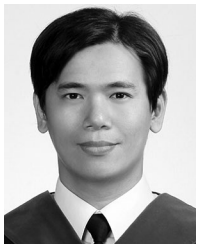

Wen-Yu Huang was born in Taiwan, R.O.C., in 1974. He received the B.S. and M.S. degrees in electrical engineering from National Taiwan Ocean University, Keelung City, Taiwan, R.O.C., and National Cheng Kung University, Tainan City, Taiwan, R.O.C., in 2002 and 2010, respectively. He is currently working toward the Ph.D. degree in electrical engineering.

His research interests include ac–dc, dc–dc power converters, PV inverters, and wireless power converters.

Wei-Jing Tseng was born in Kaohsiung, Taiwan, R.O.C., in 1981. He received the B.S., M.S., and Ph.D. degrees in electrical engineering from National Cheng-Kung University (NCKU), Tainan, Taiwan, R.O.C., in 2004, 2006, and 2015, respectively.

Since 2016, he has been a Postdoctoral Researcher with NCKU. His research interests include power electronics, linear power, switching power, and light-emitting diodes.